# High specificity targeting and detection of human neuroblastoma using multifunctional anti-GD2 iron-oxide nanoparticles

**Dana C. Baiu**[1], **Nathan S. Artz**[2], **Meghan R. McElreath**[1], **Bryan D. Menapace**[1], **Diego Hernando**[2], **Scott B. Reeder**[2], **Cordula Grüttner**[3], and **Mario Otto**[1,*]

[1]Department of Pediatrics, Division of Pediatric Hematology, Oncology and Bone Marrow Transplant, School of Medicine and Public Health, University of Wisconsin, Madison, WI

[2]Department of Radiology, Medical Physics, Biomedical Engineering, Medicine and Emergency Medicine, School of Medicine and Public Health, University of Wisconsin, Madison, WI

[3]Micromod Partikeltechnologie GmbH, Rostock, Germany

## Abstract

**Aim**—To develop biocompatible, tumor-specific multifunctional iron oxide nanoconstructs targeting neuroblastoma, an aggressive pediatric malignancy.

**Materials & methods**—Clinical-grade humanized monoclonal antibody (hu14.18K322A), designed to target GD2 antigen on neuroblastoma with reduced non-specific immune interactions, was conjugated to hydroxyethyl starch-coated iron oxide nanoparticles. Targeting capability in vitro and in vivo was assessed by immunofluorescence, electron microscopy, analytical spectrophotometry, histochemistry and magnetic resonance R2* relaxometry.

**Results**—The biocompatible nanoconstructs demonstrated high tumor-specificity in vitro and in vivo, and low background uptake in a mouse flank xenograft model. Specific accumulation in tumors enabled particle visualization and quantification by magnetic resonance R2* mapping.

**Conclusions**—Our findings support the further development towards clinical application of this anti-GD2 iron-oxide nanoconstruct as diagnostic and therapeutic scaffold for neuroblastoma and potentially other GD2 positive malignancies.

## Keywords

neuroblastoma; pediatric; iron oxide nanoparticle; anti-GD2; tumor targeted; cancer; MRI

*Corresponding author, University of Wisconsin Madison, Dept. of Pediatrics, 4153 WIMR, 1111 Highland Avenue, Madison WI 53705. motto@pediatrics.wisc.edu. +1-608-265-9645.

## Introduction

Neuroblastoma, a neural crest derived malignancy, is the most common extracranial solid tumor of childhood. It is a disease of very young children and infants, who present with a median age of 19 months at diagnosis. The majority of patients present with advanced and widely metastatic disease. Despite highly toxic multimodality therapy, which includes chemotherapy, surgery, autologous transplantation, radiation and immunotherapy, affected children experience an overall survival of only 50-55% [1]. While neuroblastoma accounts for only 7% of all pediatric cancers, it is responsible for about 15% of cancer mortality in children. In addition, patients who survive are confronted with long-term side effects of the aggressive treatment, such as secondary cancers, hearing loss and cognitive impairment. For these reasons, there is an immediate need for new and innovative treatment modalities to improve overall survival while minimizing treatment associated morbidities.

The evolution of nanotechnology opens a new dimension in tumor-targeted therapeutic strategies. In particular iron oxide (IO) based nanoparticles have gained increasing interest for medical applications due to their high stability and biological compatibility, controllable morphology and size dispersion, as well as chemical surface functionalization. Furthermore, their magnetic properties permit visualization with magnetic resonance (MR) imaging, which is a safety imaging modality that uses no ionizing radiation [2]. Further, when placed in alternating magnetic fields, magnetic nanoparticles generate heat, a property that can be exploited in hyperthermia cancer treatment [3]. Taken together, these properties allow for sophisticated molecular tumor targeting packaged in a smallsize drug delivery system. However, few experimental IO based nanosystems have been developed that are highly tumor specific, retain their biocompatibility and can be visualized by MR imaging after intravenous injection. Furthermore, none has reached clinical trial stage or would be relevant to childhood cancers [4].

The potency of a tumor-targeting nanoconstruct to deliver a therapeutic load depends on many criteria. Important factors that characterize nanoparticle include their size and narrow size distribution, surface functionalization allowing for effective antibody coupling, the magnetic properties for imaging and hyperthermia applications, and overall biocompatibility to allow for sufficient circulation time in the blood. The targeting capacity is determined by the tumor specificity of the targeting moiety, such as an antibody, as well as efficacious but gentle bioconjugation methods to preserve epitope recognition and biocompatibility of the nanoconstruct. To this end, we aimed to design a biocompatible nanoparticle scaffold using nanoferrite particles conjugated to the clinical grade humanized antibody hu14.18K322A to target the disialoganglioside GD2 on neuroblastoma. GD2 is highly expressed by tumors of neuroectodermal origin. Almost 95% of neuroblastomas consistently express the GD2 antigen, while only low levels are detected on healthy tissues [5, 6]. Development and subsequent evolution of therapeutic anti-GD2 antibodies and their integration into upfront treatment regimens have had a remarkable impact on the outcome of neuroblastoma, underscoring the targeting capability of these molecules [7]. For our nanoconstruct, we chose the humanized antibody hu14.18K322A as targeting moiety. We have previously shown that hu14.18K322A is a clinically relevant humanized anti-GD2 antibody engineered to decrease the ability to interact with complement factor C1q (through a K322A point

mutation), thereby greatly increasing its tolerability while preserving target affinity [8]. We recently published first-in-human studies using this antibody in pediatric patients with refractory neuroblastoma [9]. To generate a tumor-targeted nanoconstruct, we chose cross-linked hydroxyethyl starch-coated magnetite ($Fe_3O_4$) core shell particles of 80 nm diameter as our scaffold (Bionized NanoFerrite, BNF, Micromod, Germany). These particles consistently demonstrate narrow size distribution, superb magnetic properties for imaging and heating, and have shown excellent biocompatibility in vitro and in rodent models [10, 11]. In addition, these particles have been successfully conjugated to antibodies and proved to have outstanding *in vivo* pharmacokinetics [11, 12].

We report here the efficient conjugation of BNF Starch nanoparticles to hu14.18K322A anti-GD2 antibody and results of our *in vitro* and *in vivo* targeting and imaging experiments in pre-clinical rodent xenograft models of neuroblastoma. Our data suggest that this nanoconstruct is a suitable candidate for tumor-specific targeting of neuroblastoma, with high potential to serve as a multifunctional therapeutic nanoplatform.

## Materials and methods

### Nanoconstruct preparation

BNF-Starch IO nanoparticles were synthesized by high-pressure homogenization [12]. Clinical-grade, humanized monoclonal anti-GD2 hu14.18K322A antibody was kindly provided by Children's GMP LLC, Memphis, TN. For particle functionalization, sulfo-SMCC (6.1 mg) in DMSO was added to a suspension of BNF-Starch (2.25 ml, c(Fe)= 13.6 mg/ml) in PBS-EDTA buffer (pH=7.4). After 1 hour at 20°C the excess of sulfo-SMCC was removed with PBS-EDTA in a PD-10 desalting column. The hu14.18 K322A antibody (1.67 mg/ml in PBS buffer) was thiolated with Traut's reagent (14 mM 2-iminothiolane) in PBS-EDTA for 1 h 20°C and excess of 2-iminothiolane was removed with PBS-EDTA in a G-25 desalting column. The maleimide functionalized IO particles were mixed with the thiolated antibody for 2 hours at 20°C, then remaining maleimide groups on the particle surface were quenched with 20 mM cysteine. The particles were washed three times with 0.05% Tween-20/ PBS by magnetic separation, and filtered through 0.22 μm PES. The hydrodynamic size was measured on a Zetasizer Nano-ZS90 (Malvern Instruments, Worcestershire, UK) at constant iron concentrations of 0.1 mg/ml in PBS.

### Protein assay

The conjugated antibody was measured by a modified bicinchoninic acid (BCA) method (Thermo Fisher Scientific, Germany) for 2 hours at 37°C. A calibration curve was prepared by adding increasing amounts of hu14.18K322A to aminated reference particles without antibody on the surface at a constant iron concentration of 0.25 mg/ml. The antibody-coated particles were adjusted to the same iron concentration of 0.25 mg/ml.

### Cells

Human GD2 positive ($GD2^+$) neuroblastoma cell lines CHLA-20 and NB1691 (courtesy of Dr. Andrew Davidoff, St. Jude Children Research Hospital, Memphis, TN) were cultured in IMDM (HyClone, South Logan, UT) or RPMI (Corning Cellgro, Manassas, VA)

respectively. GD2 negative (GD2$^-$) cells (human carcinoma PC-3, mouse myeloid RAW264.7, cultured in RPMI, and respectively primary isolates of infant foreskin normal fibroblasts HUFI, cultured in DMEM, Corning Cellgro) were kind gifts from Dr. Jacqueline Hank, Department of Human Oncology, and Dr. Victoria Browning, Department of Surgery, University of Wisconsin-Madison, respectively. All media were supplemented with 10% fetal bovine serum (Gibco, Grand Island, NY).

### Animal models

Animal care and use were in agreement with approved institutional protocols and NIH guidelines. Human tumor xenografts were established in immunodeficient NOD.Cg-Prkdc$^{scid}$ Il2rg$^{tm1Wjl}$/SzJ mice (Jackson Laboratory, Bar Harbor, ME), hereafter abbreviated NSG, by inoculating $4 \times 10^6$ tumor cells subcutaneously, dorsal in the flanks. Three weeks post-inoculation, nanoparticles were administered intravenously at 140 µmol Fe/kg body weight. Nanoparticle biodistribution was quantified at the specified time points by Perls histochemistry, analytical spectrophotometry, or MR imaging. Tissue samples were fixed in 4% formaldehyde for microscopy, or weighed fresh, then frozen for spectrophotometry.

### Immunofluorescence microscopy and flow cytometry

Cell suspensions in complete medium ($1.25 \times 10^7$ cells/ml) were incubated with nanoparticles (60 µg Fe/$10^6$ cells) for 1 hour at room temperature. Cell-bound nanoparticles were detected with 1 µg /ml Alexa 488-labeled goat anti-human IgG (Molecular Probes, Eugene, OR). Pre-treatment for 10 minutes of cells with 3µg/ml murine anti-GD2 antibody (clone 14.G2a, Chemicon, Temecula, CA), or pre-treatment of anti-GD2-BNF nanoconstructs with 3µg/ml purified murine antibody anti-idiotype of 14.18 antibody (clone 1A7 [13], Titan Pharmaceuticals, Scottsdale, AZ) were used for specific inhibition. Cells were spread by cytospin onto L-lysine coated glass slides and examined on a Nikon microscope Eclipse Ti-U/ DS-QiMc. Fluorescence images were pseudo-colored and merged using Nis-Elements D3.10. Alternatively, the cells in suspension were examined by flow cytometry on a MACSQuant Analyzer 10 (Miltenyi Biotec, Auburn, CA) in the presence of propidium iodide for detection of dead cells, and analyzed using FlowJo (Tree Star, Ashland, OR).

### Histochemistry

Deparaffinized tissue sections, or acetone-fixed cytospins of cells treated with nanoparticles were stained by Perls reaction and counterstained with nuclear fast red [14]. Iron, precipitated as ferrocyanide (Prussian blue) was assessed on a Nikon microscope Eclipse Ti-U/ DS-2Mv.

### Analytical spectrophotometry

Cell samples, or mouse tissue of known weight (in multiple replicates), were lysed with 0.5M NaOH (250µl for every 50mg tissue or $5 \times 10^5$ cells) for 72 hours at 10°C. After neutralization with 0.5M HCl, iron was quantified by ferrozine spectrophotometry [15]. Samples were clarified by centrifugation for 15 minutes at 17,000g. Optical densities at 570nm were assessed on a Tecan Spectra plate reader, with IO nanoparticle standard curves

for quantification. For inhibition experiments, free hu14.18K322A anti-GD2 antibody was used at 10 μg/ml.

### Transmission electron microscopy (TEM)

Ultrathin (60-90nm) sections of fixed cells in Embed 812 Resin (EMS, Hatfield PA) were evaluated on a Philips CM 120 STEM/MegaView III. For intracellular detail, some sections were treated with 8% uranyl acetate. For iron-specific staining we modified the procedure of Meguro et al [16] by substituting the silver-gold-uranyl nitrate post-DAB intensification with $NiCl_3$ and introducing a permeabilization step. Specifically, after fixation, cell monolayers were permeabilized with 0.2% Triton X-100 in cacodylate buffer for 30 minutes, stained with 3% potassium ferrocyanide in 10% HCl for 10 minutes, followed by $DAB/NiCl_3$ (Vector Labs, Burlingame, CA). After dehydration, cells were embedded in Durcupan ACM resin (Sigma-Aldrich) and etched with HF to remove the glass coverslip before ultrathin sectioning.

### Viability and proliferation assay

The cytosolic NAD(P)H-dependent cellular oxidoreductase enzyme activity was evaluated with the 3-(4,5-Dimethylthiazol-2-yl)-2,5-Diphenyltetrazolium Bromide (MTT) assay [17]. 0.3% formaldehyde in PBS was used as control of total cell death.

### Magnetic resonance (MR)

**Phantom MR**—1% agarose phantoms were prepared with varying BNF iron concentrations (0.09; 0.358; 0.627; 0.895mM). MR scanning was performed at 3T on a Discovery MR750 clinical scanner (GE Healthcare, Waukesha, WI) using a commercial eight channel wrist coil. A three-dimensional, chemical shift encoded, multi-echo spoiled gradient-echo technique was used (parameters detailed in Supplementary information). Maps of the R2* relaxation parameter (the rate of decay of MR signal across echo times) were reconstructed using fat-corrected, complex spectral modeling as we have previously described [18]. A region of interest [19] was placed on the R2* map within each vial and the mean value across pixels was recorded.

**Experimental mice MR**—Mice (n=3) were scanned sequentially pre- then 5h, 24h, or 48h post-administration of anti-GD2-BNF, or immediately following euthanasia (n=2, no treatment and 24h post-administration) using the same MR hardware as above (parameters detailed in Supplementary information). A spectral modeling-based reconstruction of the data generated R2* maps in the same manner described above, as well as images depicting MR signal generated from water. Regions of interest [19] circumscribing the GD2^{+} tumors and contralateral GD2^{−}tumors, as well as ROI demarcating skeletal muscle were defined on the co-localized water signal images. R2* measurements for each ROI were determined by averaging R2* values across all pixels within the ROI. The fold change in tissue iron content was calculated for each ROI category (tumor, muscle) by the ratio between the R2* values measured after administration of anti-GD2 BNF and the R2* values measured in the corresponding ROI before anti-GD2 BNF administration.

### Statistics

The statistical significance of the data was tested with unpaired Student's *t* test. The calculated goodness-of-fit (p value) was indicated in the figure legend. Targeting efficiency was calculated as % injected dose/g tissue, according to the formula % ID/g = (iron detected per gram of tissue by analytical spectrophotometry/injected iron dose) × 100; and per organ (organ weight × % ID/g).

## Results

### Generation and physico-chemical characterization of anti-GD2 BNF nanoparticles

BNF Starch particles with amino groups on the surface were conjugated to the hu14.18K322A antibody according to Figure 1A-C, resulting in a saturating concentration of 12 μg of hu14.18K322A bound antibody per mg of iron. After conjugation, the anti-GD2 BNF nanoconstructs presented as a monodisperse suspension (Figure 1D-E), with the same characteristics in TEM (Figure 1D) as the non-conjugated particles [3], and with the mean particle diameter increased from 88 nm (polydispersity index (PDI): 0.11) to 99 nm (PDI: 0.14) by the antibody conjugation (Figure 1E).

### Nanoconstructs bind to GD2 molecules with very high selectivity

To confirm the conserved specificity of the anti-GD2 hu14.18K322A antibody after its coupling to BNF nanoparticles, we tested the binding of anti-GD2-BNF nanoconstructs to cultured cells, using fluorescent anti-human secondary antibodies to track the particle-conjugated hu14.18K322A antibody by flow-cytometry and microscopy. Binding of anti-GD2-BNF was specific for human GD2$^+$ neuroblastoma cells, with GD2$^-$ cells (human or mouse) showing complete absence of binding (Figure 2A). The binding capacity of the anti-GD2 antibody after coupling to BNF nanoparticles was minimally decreased but comparable with antibody alone in the recognition of GD2 expressed on CHLA-20 neuroblastoma cells (Figure 2B). The fluorescence staining was not due to human anti-GD2 antibody interaction with Fc receptors on cell surfaces, since neuroblastoma cells did not bind polyclonal human IgG (Figure 2C). As an additional evidence that only the Fab portions of the anti-GD2 were implicated in the recognition of the neuroblastoma targets, pretreatment of anti-GD2-BNF nanoconstructs with 1A7 antibody specific for the anti-GD2 idiotype fully prevented the binding of the nanoconstructs to the cells (Figure 2C lower left panel). Furthermore, blocking the GD2 epitopes on the cell surface with 14G2a murine anti-GD2 antibody inhibited the subsequent binding of anti-GD2-BNF to the cells (Figure 2C lower right panel), indicating that the specificity of the hu14.18K322A antibody in the anti-GD2-BNF nanoconstructs is unaltered.

### Iron-oxide nanoparticles are targeted to GD2-expressing tumor cells

We then tested the ability of the anti-GD2 antibody to direct the IO nanoparticles to GD2$^+$ cells by measuring the iron loading of cells after nanoparticle treatment. Anti-GD2-BNF nanoconstructs specifically delivered iron to GD2$^+$ neuroblastoma cells, but not to GD2$^-$tumor or normal human lines (Figure 3A). Pretreatment of GD2$^+$ neuroblastoma cells with free hu14.18K322A antibody, by blocking the targeted molecules, significantly

inhibited cells loading with iron, attesting to the specificity of the IO nanoparticle delivery (Figure 3B, C). Non-targeted BNF did not bind to neuroblastoma cells (Figure 3B, C), excluding cell loading by passive pinocytosis as the mechanism responsible for iron uptake by cells. In conclusion, anti-GD2-BNF nanoconstructs specifically target iron oxide to GD2$^+$ neuroblastoma cells.

## After binding to cell surface GD2, the IO nanoparticles are internalized

To allow time for downstream clinical applications, after recognition of targeted receptors the nanoconstructs need to be retained for sufficient time on the tumor plasma membrane and penetrate inside the tumor cells. To study the fate of the nanoconstructs after binding to targets, cells were treated with nanoparticles at 480μg Fe/ml for 1h, unbound nanoparticles were rinsed away, and cells were cultured for 4, 12 or 18 hours at 37°C in humidified atmosphere. After 1 hour of incubation, the majority of anti-GD2-BNF nanoparticles were localized on the cell surface (Figure 4A). At 4, 12 and 18 hours multiple electron-dense particles could be revealed in the cytoplasm (exemplified for 18 hours in Figure 4B). Counterstaining for intracytoplasmic structures showed that electron-dense nanoparticles were located within vesicular structures, possibly endo-lysosomes (Figure 4C), whose contents stained positive for iron (Figure 4D). We next tested whether nanoconstruct internalization or simple contact of nanoconstructs with cells affect cell viability or growth. Following 1 hour incubation of tumor cells or primary cultures of normal skin fibroblasts with increasing concentrations of anti-GD2-BNF, the incorporation of propidium iodide did not indicate a significant decrease in cell viability (Figure 5A). Subsequent culture of the cells at optimal values for linear growth ($2 \times 10^6$ cells/ml for GD2$^+$tumor CHLA-20, and $1.5 \times 10^6$ cells/ml for GD2$^-$normal cells HUFI) for 24, 48 or 72 hours at 37°C did not indicate alterations in cell survival or proliferation (Figure 5B).

## Nanoconstructs target neuroblastoma *in vivo*

The key property of a clinically relevant tumor-targeted nanoconstruct is to maintain its tumor specificity *in vivo*. Neuroblastoma xenograft-bearing mice were administered targeted anti-GD2- BNF or non-targeted BNF at equivalent iron concentration (140 μmol Fe/kg body weight), and iron content of various organs (as a measure of nanoparticle targeting) was assessed after 24 hours. After intravenous administration of anti-GD2-BNF nanoconstructs, the accumulation of IO nanoparticles in GD2$^+$ xenografts was significantly higher than the background iron levels in tumors of non-treated mice, and than the levels in tumors of mice that received unconjugated BNF particles (Figure 6A). When anti-GD2-BNF nanoconstructs were administered to animals bearing two opposite flank xenografts, a GD2$^-$tumor (PC3 prostate cancer) and a GD2$^+$ tumor (CHLA-20 neuroblastoma), IO nanoparticles accumulated selectively in the GD2$^+$ tumor (Figure 6B, C). No other sampled tissues or organs (skeletal muscle, endocardium, kidney, brain, skin, lung, spleen, liver) displayed statistically significant higher iron accumulation in either BNF or anti-GD2-BNF treated mice, as supported by both spectrophotometry (Figure 6D, E) and histochemistry (data not shown). The biodistribution per organ, accounting for differences in average organ weight (lung 0.2g, spleen 0.03g, liver 1.5g, tumor 0.9g), indicates that most of the particles not captured by tumors were cleared from the circulation by the liver (Figure 6F) in similar proportion for targeted and non-targeted particles, and in lesser proportion by spleen. The

targeting efficiency of anti-GD2 nanoparticle to tumors was 14% (range 8-23%) of the injected dose (ID) reported to total organ weight, with 48% ID taken up by liver, 15.7% ID by spleen, and 8.7% ID by lung. In conclusion, *in vivo* intravenous administration of anti-GD2-BNF specifically targets GD2$^+$ xenografted neuroblastoma tumors, conveying to our knowledge the first evidence of successful *in vivo* targeting of neuroblastoma with IO nanoparticles.

### MR and R2* relaxometry in animal models of human neuroblastoma

Next, we investigated the use of magnetic resonance to probe the nanoparticle accumulation in tumors. We used the rate of decay of MR signal (R2*), which has demonstrated strong correlation with the iron concentration in phantoms and tissue [20, 21]. Scanning phantoms of BNF nanoparticles revealed an excellent linear correlation between BNF concentration and R2* (Figure 7A). To determine whether MR-based R2* relaxation measurements detect differences between IO nanoparticle accumulation in different tissues, 3T MR acquisitions were performed in xenografted mice. In agreement with the histology and the iron quantification data presented above, at 24 hours after nanoparticle administration R2* measurements indicated higher accumulation of iron in the GD2$^+$ tumors resulting in over 2 fold increase of R2* values in mice that received nanoparticles when compared with R2* of control mice with no treatment (Figure 7B, C). In addition, accumulation in the contralateral GD2$^-$ tumor as well as in skeletal muscle was minor. Accumulation of anti-GD2-BNF at the GD2$^+$ tumor site was detectable by MR at 5 hours and still present at 48 hours post-injection, but at lower levels (not shown). In summary, the MR data strongly support the high selectivity of anti-GD2-BNF nanoconstructs for GD2$^+$ neuroblastoma tumors. Our data indicate that the magnetic properties of anti-GD2-BNF combined with the high sensitivity of R2* mapping allow the visualization and quantification of the effect of the iron nanoconstruct accumulation in targeted tumors.

## Discussion

The objective of our study was to design an iron oxide (IO) nanoconstruct for the non-invasive targeting of high-risk neuroblastoma. In particular, we sought to develop a construct with high specificity for tumors paralleled by low uptake in non-tumoral tissue, and characterized by stability, biocompatibility and good imaging properties for particle detection by MR. We provide here evidence that anti-GD2 BNF IO nanoparticles with a coating of cross-linked hydroxyethyl starch bind to GD2-expressing neuroblastoma cells, and accumulate in GD2 positive neuroblastoma tumors *in vivo* with high specificity after intravenous administration. Secondly, we show that anti-GD2 BNF nanoconstructs are internalized by neuroblastoma cells, and neither their internalization nor their contact with normal cells induce cell death. Finally, our data show that anti-GD2 BNF nanoparticles targeting human pediatric neuroblastoma tumors can be visualized and detected by MR in a murine flank xenograft model.

Target specificity is a fundamental requirement for a targeted nanoconstruct to be suitable for diagnostic or therapeutic applications in oncology. The nanoconstruct we designed targets GD2, a cell surface disialoganglioside highly expressed by neuroectoderm-derived

tumors (such as neuroblastoma, melanoma, brain tumors), and by a variety of sarcomas [5, 22-24]. On healthy tissue, GD2 expression is restricted to the cerebellum and peripheral nerves at low levels [6]. This distinctively high expression on tumor cells compared with normal cells makes GD2 a prime candidate for cancer-targeted therapies in oncology. Our previous data on screening antibodies raised against GD2 indicated that hu14.18K322A displays exceptionally high specificity and hence, has an excellent potential for cancer immunotherapy [9]. Originally developed as a murine antibody (14.18) [5], then modified to a chimeric form (ch14.18) [7, 25], the antibody has recently been humanized (hu14.18) [26]. Ch14.18 (Unituxin®) has recently received FDA approval for the treatment of neuroblastoma, and is only the third drug in more than 20 years to receive initial FDA approval to treat a pediatric cancer. Hu14.18 reached phase II trials for relapsed/refractory neuroblastoma [27] and metastatic melanoma [28]. Additionally, since allodynia due to hypersensitivity reactions triggered by peripheral nerve GD2 molecule expression was reported in clinical trials, hu14.18 has been recently engineered to evade the interaction with complement factor C1q through the introduction of a point mutation (K322A), greatly reducing its dose-limiting side effects in the clinic [9]. Based on its high tumor specificity and favorable clinical trial data we chose to use clinical grade hu14.18K322A as a targeting moiety for the development of our nanoconstruct.

Thiolation of the hu14.18K322A antibody followed by its coupling to maleimide functionalized BNF particles did not affect the antibody's high specificity for $GD2^+$ neuroblastoma cells, as demonstrated by flow cytometry and immunohistochemistry methods. The recognition of the GD2 molecules by the nanoconstructs was based exclusively on the interaction between the antibody Fab variable region and the GD2 epitope, as it was efficiently blocked when free anti-GD2 antibodies were used to mask the GD2 epitopes, or when anti-idiotype antibodies were used to block the construct's Fab regions (Figures 2 and 3). More importantly, the high specificity of the anti-GD2-nanoconstructs for human neuroblastoma tumors was maintained *in vivo* in our preclinical models of $GD2^+$ tumors: after intravenous administration to xenografted animal models, the nanoparticles accumulated specifically in the human neuroblastoma tumors and were detectable and measurable by histochemistry, analytical spectrophotometry and magnetic resonance (Figures 6 and 7). Besides $GD2^+$ tumors which captured GD2-targeted nanoparticles, no other tissue showed statistically significant retention of the antibody conjugated nanoparticles or of the non-conjugated particles (Figure 6). These data suggest that the serum levels of the anti-GD2 targeted nanoparticles allowed them sufficient time to access $GD2^+$ tumor cells through inter-endothelial cell gaps (300-4700nm diameter) of defective tumor capillaries [29]. Once passing in the intratumoral space, the nanoparticles likely engaged in anti-GD2–GD2 interactions, which resulted in their specific retention at the tumor site. The accumulation was GD2-specific and not solely due to an enhanced permeability and retention (EPR) effect of poorly structured tumor neovasculature and defective lymphatic drainage [30], because non-targeted nanoconstructs did not accumulate in $GD2^+$ or in $GD2^-$ tumors, and anti-GD2-BNF did not accumulate in $GD2^-$ tumors (Figure 6). With an average targeting efficiency to specific tumors of 14% ID per tumor weight (35% ID/g), anti-GD2 nanoparticles fare among the highest efficiency targeted nanoparticles in their size range [31], providing sufficient intratumoral bioavailability for therapeutic or

diagnostic applications. Since the potential use of IO-nanoconstructs as drug carriers or as tumor thermoablation probes relies greatly on the delivery and retention of the cargo or thermodynamic effect at the tumor site, our promising data suggest that anti-GD2-BNF may be utilized in the future as therapeutic nanocarriers.

In addition to targeting and retention in tumor, a delayed or minimal clearance of circulating particles by the mononuclear phagocytic system is essential to allow for sufficient circulation time and subsequent tumor targeting. While anti-GD2-BNF nanoparticles were preferentially captured by GD2$^+$ xenograft tumors (3.2 fold increase over constitutive iron levels/ g tissue, Figure 6A), the liver accounted next for the largest uptake of iron (1.9 fold increase), with a tumor-to-liver % ID/g ratio of 0.30, only marginally better than the generally reported average of 0.28 [31], and lastly, the spleen (1.5 fold increase, Figure 6D). The retention of the anti-GD2 antibody-conjugated BNF in liver and spleen was not significantly different from that of non-targeted BNF (Figure 6D, E), suggesting that the interaction of the hu14.18K322A antibody Fc domains with macrophage or dendritic cell Fc receptors is unlikely to play a significant role in the clearance of anti-GD2-BNF particles by spleen or liver in our model. This is supported by the observed marginal binding of anti-GD2-BNF by the GD2 negative macrophage cell line RAW264.7 (Figures 2-3), a cell line reported to express functional Fc receptors [32] and able to internalize iron oxide nanoparticles by receptor mediated endocytosis [33]. Two other uptake mechanisms previously reported to be involved in nanoparticle clearance by liver and spleen phagocytic system [4, 34], might account for the observed BNF and anti-GD2-BNF uptake by spleen and liver cells: scavenger receptor mediated endocytosis, and complement receptor binding followed by macropinocytosis. With regard to complement binding, we have previously shown that the K322A mutated version of hu14.18 (hu14.18K322A) impairs the assembly of the classical complement cascade [8], thus by utilizing hu14.18K322A as targeting moiety we expect the anti-GD2-BNF nanoconstructs to have a decreased capacity to bind C1q and consequently C3b. Additionally, we expect the cross-linked starch coating of the particles to decrease esterification with complement C3b, since cross-linking of free hydroxyls was shown to greatly prevent opsonization of nanoparticles with complement, decrease their uptake by liver macrophages, and increase by 10-fold their serum half-life [35]. Altogether, these modifications have the potential to translate into reduced opsonization of BNF and anti-GD2-BNF particles by complement and decreased particle macropinocytosis by macrophages. These properties might therefore account for the absence of significant differences between the uptake of targeted and non-targeted particles by liver and spleen, and sufficient circulation times in the blood flow for the targeted anti-GD2-BNF particles to reach the tumor targets with high efficiency. Although inevitable, the clearance of particulate constructs by the reticuloendothelial system may be delayed by additional nanoparticle engineering, with the scope of maximizing their serum half-life, which will increase their bioavailability in the tumor and broaden their therapeutic window. Future research will address preclinical pharmacokinetics of the GD2-targeted nanoconstructs to identify the optimal dose for attaining maximal intratumoral bioavailability for therapeutic or diagnostic applications, with minimum clearance by the reticuloendothelial system.

Besides the critical requirement for tumor target specificity, of equal importance in cancer therapy, especially in a pediatric setting, is the biocompatibility of nanoconstructs. The

majority of anti-cancer agents that could serve as therapeutic load for nanocarriers elicit their effect by targeting intracellular processes or interference with DNA [36]. From a therapeutic point of view, it is therefore desirable for the molecular targets to mediate the internalization of the nanoparticles for subsequent drug release. Our data indicate internalization with a slow rate of the anti-GD2 nanoparticles after specifically binding to GD2 molecules on neuroblastoma cells, as evidenced by the presence of electron-dense structures in the cell cytoplasm by TEM 12-18 hours (Figure 4) after treatment, and less so at 4 hours (not shown). The kinetics are consistent with mechanisms of cell surface molecule recycling and pinocytosis rather than active receptor-mediated endocytosis, in agreement with previous reports of slow kinetics of internalization of hu14.18-IL-2 recombinant molecules bound to surface GD2 on melanoma tumor cells [37]. Future experiments will address dosing and pharmacokinetics to determine the optimal number of particles to be administered in order to achieve sufficient delivery of an effective therapeutic load to tumors. Internalization of IO crystals lacking appropriate protection by coating polymers after treatment of macrophage cell lines at concentrations above 300μg/ml was previously reported to induce cytotoxicity [38]. Our *in vitro* experiments, using either tumor or normal human cells treated with variable amounts of anti-GD2-BNF nanoconstructs bearing the maximum number of antibody molecules per particle attainable in the chemical coupling conditions specified, did not show cell viability alterations in the short term, or long term after multiple days in culture, indicating that cell contact, specific binding, or even internalization of anti-GD2-BNF nanoconstructs are not cytotoxic and do not impair cell proliferation, even at concentrations up to 480 μg Fe/ml (Figure 5).

Finally, in this study R2* relaxometry (parametric fitting to obtain a map of the spatial R2* distribution) was used to assess iron oxide nanoparticle accumulation in neuroblastoma xenografts after anti-GD2-BNF intravenous injection. We have chosen BNF particles with a coating of hydroxyethyl starch because they have shown advantageous properties as contrast agents in MR imaging and magnetic hyperthermia in comparison to other magnetic nanoparticles used for biomedical applications, such as nanomag®-D-spio, nanomag®-CLD-spio, and the clinically approved IO nanoparticles Feridex® [3, 39]. Previously published reports of various tumor specific IO nanoconstructs, targeted *in vivo* to underglycosylated mucin-1 (MUC-1) epithelial tumor antigen [40], folate receptors on lung carcinoma [41], pancreatic tumor EGF receptors [42], luteinizing hormone-releasing hormone receptors (LHRH-R) on breast metastases [43], and prostate cancers secreted protein acidic and rich in cysteine (SPARC glycoprotein) [44], have all relied on T2-weighed images to visualize the localization of IO nanoconstructs in the tumor by MR. An exception was provided by Lee et al [45] who used R2 measurements overimposed on T2-weighted MR images to visualize and determine the increase in anti-EGFR IO nanoparticle deposition in breast cancer xenografts. Unfortunately, T2 imaging and R2 mapping rely on relatively slow spin-echo based MR imaging, which complicates their potential clinical application. On the other hand, the R2* decay rate is also highly sensitive to the presence of tissue iron, but R2* mapping can be performed with very rapid gradient-echo acquisitions [21], essential for clinical applications, particularly in pediatric patient populations. We therefore applied an R2* relaxometry MR approach for the non-invasive visualization and quantification of the effect of anti-GD2-BNF nanoparticle accumulation in tumors. The R2* results confirmed

the spectrometry and histochemistry data of specific targeting of GD2 positive tumor by anti-GD2 nanoconstructs and suggest that MR is well suited for assessing anti-GD2-BNF localization and concentration in animal models of human neuroblastoma. Future preclinical imaging studies will focus on the ability of the nanoconstructs to detect neuroblastoma tumors in heterotopic and orthotopic locations.

In conclusion, our report provides a first line of evidence that BNF iron oxide nanoparticles conjugated to the clinically relevant antibody hu14.18K322A are able to target human neuroblastoma with high specificity and at levels detectable by MR in a mouse xenograft model. Hu14.18K322A is currently used in several ongoing clinical trials, and based on favorable results it will vastly expand its preclinical and clinical use. It is conceivable that, besides neuroblastoma, other GD2 positive malignancies, such as melanoma, subsets of lung cancer and osteosarcomas, may be targeted as well by the anti-GD2-BNF nanoconstruct. Bioconjugation of these "off the shelf" nanoparticles with tumor-targeted antibody is facile and can be accomplished GMP-grade. Additionally, this biocompatible and versatile nanoconstruct has the potential to serve as a multifunctional drug delivery vehicle. Further advances in magnetic resonance applications, such as alternating magnetic field (AMF) induced hyperthermia, will add to the multifunctionality of anti-GD2-BNF nanoparticles. The BNF nanoparticles used in this study possess a high specific absorption rate in 150kHz alternating magnetic fields and have already been shown to kill tumor cells through hyperthermia in vitro [3, 39] and in vivo in the context of direct intratumoral injections [46]. Their magnetic properties might be successfully exploited as therapeutic approaches in neuroblastoma and other GD2-positive malignancies.

## Supplementary Material

Refer to Web version on PubMed Central for supplementary material.

## Acknowledgments

## References

1. Maris JM. Recent advances in neuroblastoma. The New England journal of medicine. 2010; 362(23):2202–2211. [PubMed: 20558371]

2. Wood JC, Enriquez C, Ghugre N, et al. Mri r2 and r2* mapping accurately estimates hepatic iron concentration in transfusion-dependent thalassemia and sickle cell disease patients. Blood. 2005; 106(4):1460–1465. [PubMed: 15860670]

3. Bordelon DE, Cornejo C, Gruttner C, Westphal F, Deweese TL, Ivkov R. Magnetic nanoparticle heating efficiency reveals magneto-structural differences when characterized with wide ranging and high amplitude alternating magnetic fields. J Appl Phys. 2011; 109(12)

4. Baiu DC, Brazel CS, Bao Y, Otto M. Interactions of iron oxide nanoparticles with the immune system: Challenges and opportunities for their use in nano-oncology. Current pharmaceutical design. 2013; 19(37):6606–6621. [PubMed: 23621531]

5. Mujoo K, Cheresh DA, Yang HM, Reisfeld RA. Disialoganglioside gd2 on human neuroblastoma cells: Target antigen for monoclonal antibody-mediated cytolysis and suppression of tumor growth. Cancer Res. 1987; 47(4):1098–1104. [PubMed: 3100030]

6. Zhang SL, Cordoncardo C, Zhang HS, et al. Selection of tumor antigens as targets for immune attack using immunohistochemistry .1. Focus on gangliosides. International Journal of Cancer. 1997; 73(1):42–49. [PubMed: 9334808]

7. Yu AL, Gilman AL, Ozkaynak MF, et al. Anti-gd2 antibody with gm-csf, interleukin-2, and isotretinoin for neuroblastoma. N Engl J Med. 2010; 363(14):1324–1334. [PubMed: 20879881]

8. Sorkin L, Otto M, Baldwin WR, et al. Anti-gd(2) with an fc point mutation reduces complement fixation and decreases antibody-induced allodynia. Pain. 2010; 149(1):135–142. [PubMed: 20171010]

9. Navid F, Sondel PM, Barfield R, et al. Phase i trial of a novel anti-gd2 monoclonal antibody, hu14.18k322a, designed to decrease toxicity in children with refractory or recurrent neuroblastoma. J Clin Oncol. 2014; 32(14):1445–1452. [PubMed: 24711551]

10. Giustini AJ, Perreard I, Rauwerdink AM, Hoopes PJ, Weaver JB. Noninvasive assessment of magnetic nanoparticle-cancer cell interactions. Integrative biology : quantitative biosciences from nano to macro. 2012; 4(10):1283–1288. [PubMed: 22945022]

11. Natarajan A, Xiong CY, Gruettner C, Denardo GL, Denardo SJ. Development of multivalent radioimmunonanoparticles for cancer imaging and therapy. Cancer biotherapy & radiopharmaceuticals. 2008; 23(1):82–91. [PubMed: 18298332]

12. Gruttner C, Muller K, Teller J, Westphal F, Foreman A, Ivkov R. Synthesis and antibody conjugation of magnetic nanoparticles with improved specific power absorption rates for alternating magnetic field cancer therapy. Journal of Magnetism and Magnetic Materials. 2007; 311(1):181–186.

13. Sen G, Chakraborty M, Foon KA, Reisfeld RA, Bhattacharyachatterjee M. Preclinical evaluation in nonhuman primates of murine monoclonal anti-idiotype antibody that mimics the disialoganglioside gd2. Clinical Cancer Research. 1997; 3(11):1969–1976. [PubMed: 9815586]

14. Edna B, Prophet BM, Arrington Jacquelyn B, Sobin Leslie H. Laboratory methods in histotechnology. Armed Forces Institute of Pathology. 1992; 19:152.

15. Riemer J, Hoepken HH, Czerwinska H, Robinson SR, Dringen R. Colorimetric ferrozine-based assay for the quantitation of iron in cultured cells. Anal Biochem. 2004; 331(2):370–375. [PubMed: 15265744]

16. Meguro R, Asano Y, Odagiri S, Li C, Iwatsuki H, Shoumura K. Nonheme-iron histochemistry for light and electron microscopy: A historical, theoretical and technical review. Archives of histology and cytology. 2007; 70(1):1–19. [PubMed: 17558140]

17. Sylvester PW. Optimization of the tetrazolium dye (mtt) colorimetric assay for cellular growth and viability. Methods Mol Biol. 2011; 716:157–168. [PubMed: 21318905]

18. Hernando D, Kramer JH, Reeder SB. Multipeak fat-corrected complex r2*relaxometry: Theory, optimization, and clinical validation. Magnetic Resonance in Medicine. 2013; 70(5):1319–1331. [PubMed: 23359327]

19. Duewell P, Kono H, Rayner KJ, et al. Nlrp3 inflammasomes are required for atherogenesis and activated by cholesterol crystals. Nature. 2010; 464(7293):1357–1361. [PubMed: 20428172]

20. Sirlin CB, Reeder SB. Magnetic resonance imaging quantification of liver iron. Magn Reson Imaging Clin N Am. 2010; 18(3):359–+. [PubMed: 21094445]

21. Hernando D, Levin YS, Sirlin CB, Reeder SB. Quantification of liver iron with mri: State of the art and remaining challenges. J Magn Reson Imaging. 2014; 40(5):1003–1021. [PubMed: 24585403]

22. Cheresh DA, Pierschbacher MD, Herzig MA, Mujoo K. Disialogangliosides gd2 and gd3 are involved in the attachment of human melanoma and neuroblastoma cells to extracellular matrix proteins. The Journal of cell biology. 1986; 102(3):688–696. [PubMed: 3005335]

23. Cheung NK, Saarinen UM, Neely JE, Landmeier B, Donovan D, Coccia PF. Monoclonal antibodies to a glycolipid antigen on human neuroblastoma cells. Cancer Res. 1985; 45(6):2642–2649. [PubMed: 2580625]

24. Chang HR, Cordon-Cardo C, Houghton AN, Cheung NK, Brennan MF. Expression of disialogangliosides gd2 and gd3 on human soft tissue sarcomas. Cancer. 1992; 70(3):633–638. [PubMed: 1623478]

25. Mueller BM, Romerdahl CA, Gillies SD, Reisfeld RA. Enhancement of antibody-dependent cytotoxicity with a chimeric anti-gd2 antibody. J Immunol. 1990; 144(4):1382–1386. [PubMed: 2303711]

26. King DM, Albertini MR, Schalch H, et al. Phase i clinical trial of the immunocytokine emd 273063 in melanoma patients. J Clin Oncol. 2004; 22(22):4463–4473. [PubMed: 15483010]

27. Shusterman S, London WB, Gillies SD, et al. Antitumor activity of hu14.18-il2 in patients with relapsed/refractory neuroblastoma: A children's oncology group (cog) phase ii study. J Clin Oncol. 2010; 28(33):4969–4975. [PubMed: 20921469]

28. Albertini MR, Hank JA, Gadbaw B, et al. Phase ii trial of hu14.18-il2 for patients with metastatic melanoma. Cancer Immunol Immunother. 2012; 61(12):2261–2271. [PubMed: 22678096]

29. Hashizume H, Baluk P, Morikawa S, et al. Openings between defective endothelial cells explain tumor vessel leakiness. American Journal of Pathology. 2000; 156(4):1363–1380. [PubMed: 10751361]

30. Iyer AK, Khaled G, Fang J, Maeda H. Exploiting the enhanced permeability and retention effect for tumor targeting. Drug discovery today. 2006; 11(17-18):812–818. [PubMed: 16935749]

31. Yu M, Zheng J. Clearance pathways and tumor targeting of imaging nanoparticles. ACS Nano. 2015

32. Larsen EK, Nielsen T, Wittenborn T, et al. Size-dependent accumulation of pegylated silane-coated magnetic iron oxide nanoparticles in murine tumors. ACS Nano. 2009; 3(7):1947–1951. [PubMed: 19572620]

33. Gu J, Xu H, Han Y, et al. The internalization pathway, metabolic fate and biological effect of superparamagnetic iron oxide nanoparticles in the macrophage-like raw264.7 cell. Science China Life sciences. 2011; 54(9):793–805. [PubMed: 21922429]

34. Patel PC, Harrison RE. Membrane ruffles capture c3bi-opsonized particles in activated macrophages. Molecular biology of the cell. 2008; 19(11):4628–4639. [PubMed: 18768756]

35. Karmali PP, Chao Y, Park JH, et al. Different effect of hydrogelation on antifouling and circulation properties of dextran-iron oxide nanoparticles. Mol Pharm. 2012; 9(3):539–545. [PubMed: 22243419]

36. Zhao Y, Butler EB, Tan M. Targeting cellular metabolism to improve cancer therapeutics. Cell death & disease. 2013; 4:e532. [PubMed: 23470539]

37. Buhtoiarov IN, Neal ZC, Gan J, et al. Differential internalization of hu14.18-il2 immunocytokine by nk and tumor cell: Impact on conjugation, cytotoxicity, and targeting. J Leukoc Biol. 2011; 89(4):625–638. [PubMed: 21248148]

38. Naqvi S, Samim M, Abdin M, et al. Concentration-dependent toxicity of iron oxide nanoparticles mediated by increased oxidative stress. Int J Nanomedicine. 2010; 5:983–989. [PubMed: 21187917]

39. Wabler M, Zhu WL, Hedayati M, et al. Magnetic resonance imaging contrast of iron oxide nanoparticles developed for hyperthermia is dominated by iron content. Int J Hyperther. 2014; 30(3):192–200.

40. Moore A, Medarova Z, Potthast A, Dai GP. In vivo targeting of underglycosylated muc-1 tumor antigen using a multimodal imaging probe. Cancer Res. 2004; 64(5):1821–1827. [PubMed: 14996745]

41. Choi H, Choi SR, Zhou R, Kung HF, Chen IW. Iron oxide nanoparticles as magnetic resonance contrast agent for tumor imaging via folate receptor-targeted delivery. Academic radiology. 2004; 11(9):996–1004. [PubMed: 15350580]

42. Yang L, Mao H, Wang YA, et al. Single chain epidermal growth factor receptor antibody conjugated nanoparticles for in vivo tumor targeting and imaging. Small. 2009; 5(2):235–243. [PubMed: 19089838]

43. Branca RT, Cleveland ZI, Fubara B, et al. Molecular mri for sensitive and specific detection of lung metastases. Proc Natl Acad Sci U S A. 2010; 107(8):3693–3697. [PubMed: 20142483]

44. Ghosh D, Lee Y, Thomas S, et al. M13-templated magnetic nanoparticles for targeted in vivo imaging of prostate cancer. Nat Nanotechnol. 2012; 7(10):677–682. [PubMed: 22983492]

45. Lee JH, Huh YM, Jun YW, et al. Artificially engineered magnetic nanoparticles for ultra-sensitive molecular imaging. Nat Med. 2007; 13(1):95–99. [PubMed: 17187073]

46. Dennis CL, Jackson AJ, Borchers JA, et al. Nearly complete regression of tumors via collective behavior of magnetic nanoparticles in hyperthermia. Nanotechnology. 2009; 20(39)

**Executive Summary**

**Background**

- Neuroblastoma is the most common extracranial solid tumor in young children, frequently presenting with poor overall prognosis.

- Specific cancer detection tools and targeted therapies are urgently needed, especially for this fragile patient population.

**Aim**

- The development of a multifunctional, biocompatible iron oxide nanoconstruct for in vivo targeting of high-risk neuroblastoma.

**Results**

- The constructs were developed by maleimide surface functionalization of a nanoferrite hydroxyethyl-starch nanocarrier, coupled to the thiolated clinical-grade humanized monoclonal anti-GD2 antibody hu14.18K322A.

- The nanoconstructs bind with high specificity GD2-expressing neuroblastoma cells, and accumulate in GD2 positive neuroblastoma tumors *in vivo* after intravenous administration.

- The constructs are biocompatible and are internalized by neuroblastoma cells.

- The nanoparticles targeting human neuroblastoma tumors can be visualized and quantified by magnetic resonance in a murine flank xenograft model.

**Conclusions and future perspectives**

- This nanoconstruct is a suitable candidate for tumor-specific targeting of pediatric neuroblastoma with high potential to operate as a multifunctional therapeutic nanoplatform.
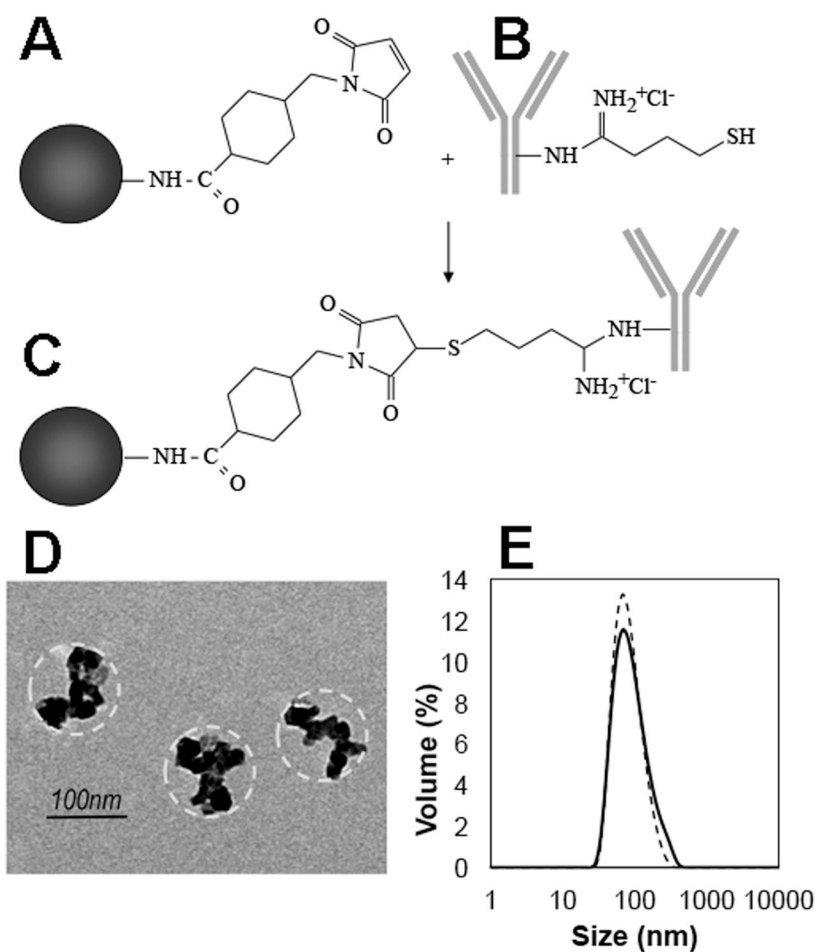
**Figure 1. Anti-GD2 nanoconstructs design and characterization**
Schematic procedure of the BNF-Starch antibody conjugation with hu14.18K322A: **A.** Maleimide modification of aminated BNF-Starch after reaction with sulfo-SMCC. **B.** Thiolation of hu14.18K322A antibody after reaction with 2-iminothiolane-HCl. **C.** Coupled maleimide modified BNF-Starch with the thiolated hu14.18K322A antibody. **D.** TEM of anti-GD2-BNF nanoparticles. Dashed line outlines the hydroxyethyl starch coating. **E.** Size distributions of BNF-Starch particles before and after antibody (representative of 5 batches).
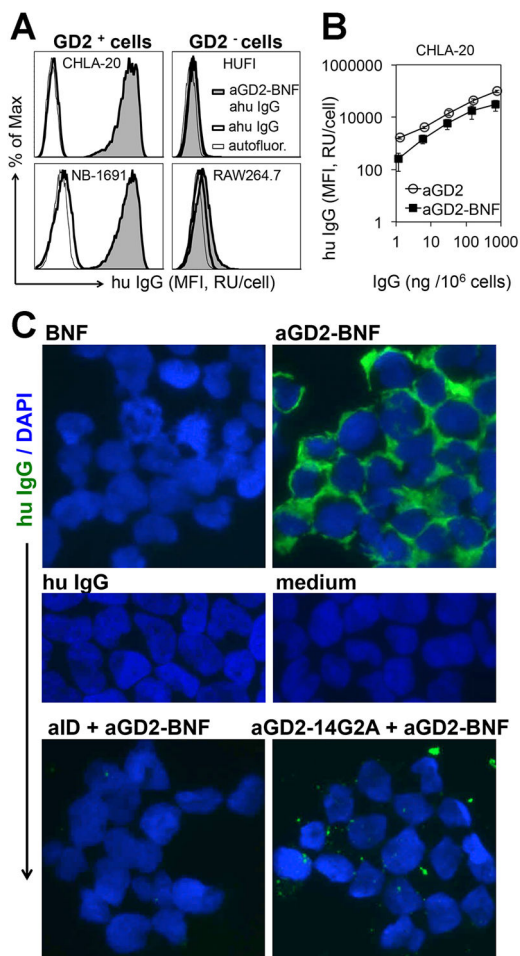
**Figure 2. Anti-GD2 nanoconstructs are highly specific for GD2 molecules on neuroblastoma cells**
**A.** Flow cytometry of anti-GD2-BNF (aGD2-BNF) binding to GD2$^+$ neuroblastoma cells, evidenced by fluorescent anti-human IgG (ahu IgG) antibody (tinted histograms), compared to cells treated with ahu IgG antibody alone (heavy contour clear histograms) or cell autofluorescence (autofluor., light contour clear histograms). **B.** Flow cytometry of anti-GD2-BNF or anti-GD2 hu14.18K322A alone binding to GD2$^+$ CHLA-20 cells. **C.** Immunofluorescence microscopy (400×) of CHLA-20 detecting hu IgG and nuclear DAPI. Cells were pre-treated with BNF, anti-GD2-BNF, human IgG (hu IgG), or medium only (upper four panels). Pretreatment with 1A7 anti-idiotype antibody (aID) or with 14G2A anti-GD2 antibody (aGD2-14G2A) prevents binding of anti-GD2-BNF to cells (lower two panels). Representative histograms and images, 4 experimental repeats. MFI, mean fluorescence intensity; RU, relative units.
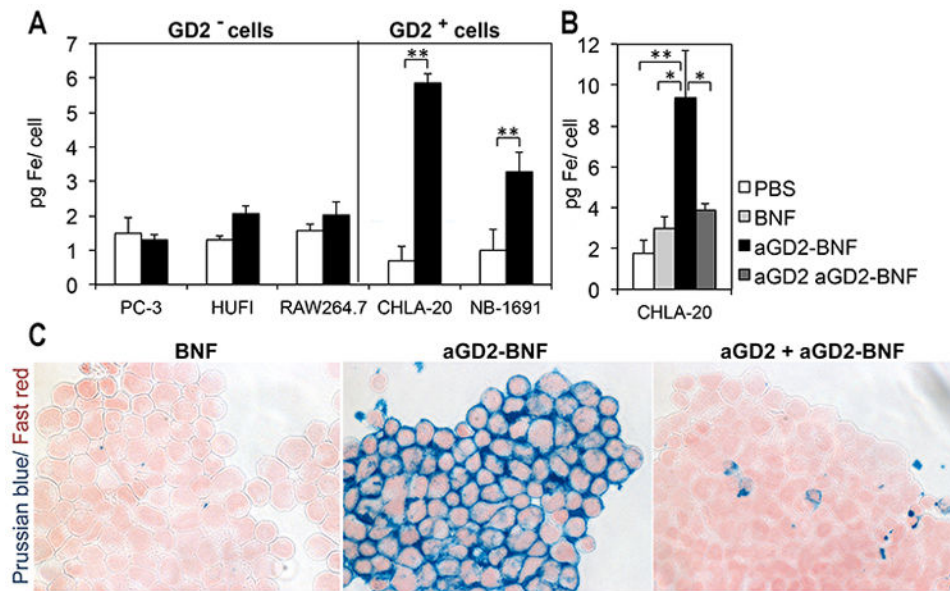
**Figure 3. Iron is targeted to GD2$^+$ neuroblastoma cells after anti-GD2-BNF treatment**
**A**. Ferrozine spectrophotometry shows increase in Fe$^{2+}$/Fe$^{3+}$ in GD2$^+$ cells after anti-GD2-BNF (aGD2-BNF) treatment when compared with basal iron levels. Averages ± SE of 3-5 experiments per cell line. **p=0.01 **B**. Ferrozine spectrophotometry shows pretreatment of CHLA-20 cells with free hu14.18K322A anti-GD2 antibody (aGD2) prevents cell loading with iron during anti-GD2-BNF treatment. Averages ± SE of 4 experiments; *p  0.04; **p=0.01. **C**. Microscopy of Perls staining of non-heme iron in CHLA-20 cells after treatment with untargeted BNF, targeted anti-GD2-BNF, and free hu14.18K322A anti-GD2 antibody (aGD2) pretreatment before anti-GD2-BNF. Representative of 5 repeats. 200×.
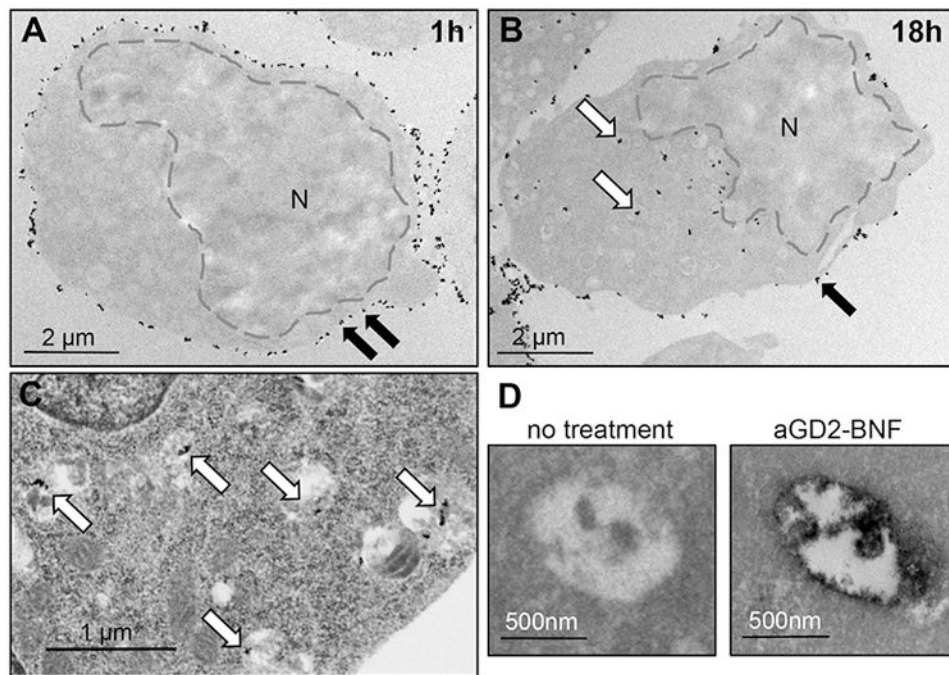
**Figure 4. Iron oxide nanoparticles are internalized after anti-GD2-BNF treatment of neuroblastoma cells**

TEM of CHLA-20 cells shows membrane-bound nanoconstructs (**A**, black arrows) after 1h incubation with anti-GD2-BNF, and intracitoplasmic nanoconstructs (**B**, white arrows) after 18h. N, nucleus. **C**. $OsO_4$ counterstained TEM shows intravesicular electron dense nanoparticles (white arrows) in CHLA-20 after 18h. **D.** Iron staining TEM of intravesicular contents after 18h culture of CHLA-20 cells treated or not with anti-GD2-BNF. Representative images of 2 experimental repeats.
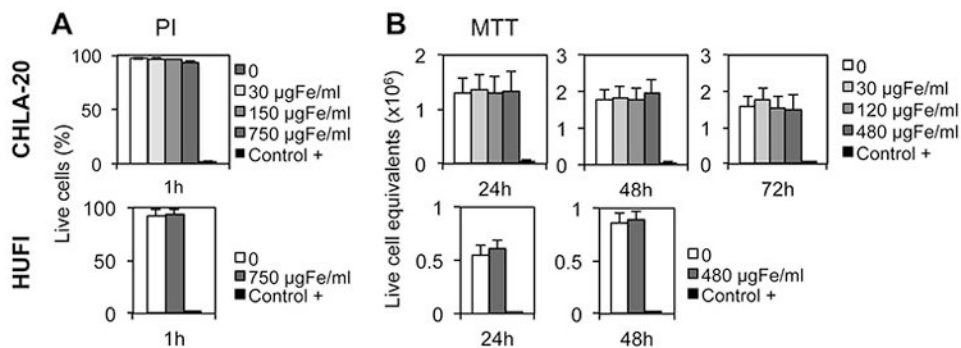
**Figure 5. Anti-GD2-BNF nanoconstructs are biocompatible**

**A**. Flow cytometry of cell viability by propidium iodide (PI) exclusion after 1h treatment with various concentrations of anti-GD2-BNF. **B**. MTT assay of cell viability after 1-3 days of culture at 37°C following treatment of cells with various concentrations of anti-GD2-BNF. Positive control (+) for cell death 0.3% formaldehyde. Averages ± SD of 3 experiments.
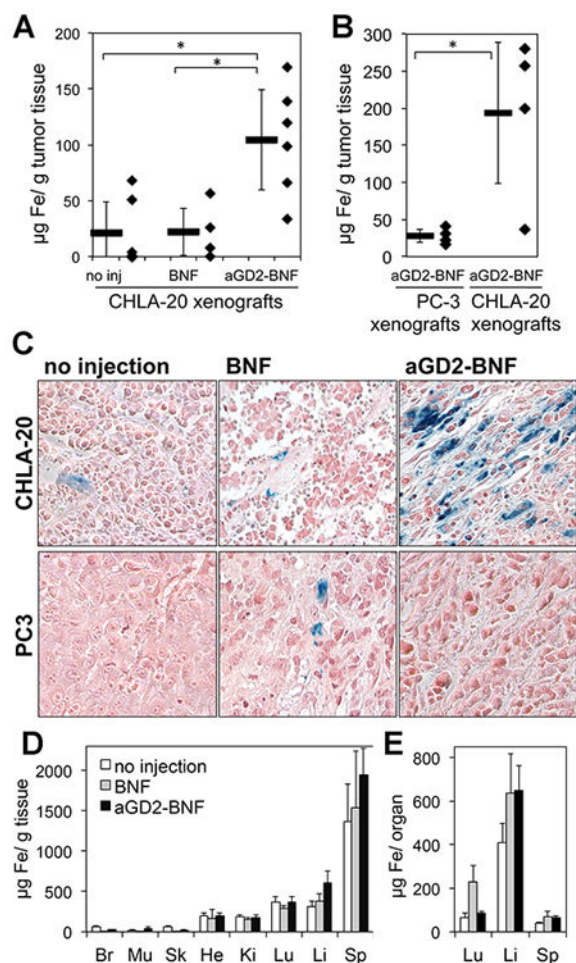
**Figure 6. Iron accumulates in GD2 positive xenografts after intravenous anti-GD2-BNF administration**

**A.** Spectrophotometry of iron content in GD2 positive tumors (CHLA-20) in mice that received no injections (no inj), or received an IV injection of non-targeted nanoparticles (BNF), or of anti-GD2-BNF (aGD2-BNF) nanoparticles 24h earlier. Average ± SE n=6, 4, and 6 respectively; *p   0.02. **B.** Spectrophotometry of iron content in tumors 24h after IV injection of anti-GD2-BNF in mice bearing flank xenografts of both GD2 negative tumors (PC3) and GD2 positive tumors (CHLA-20) *p=0.03; n=4. **C.** Histochemistry of non-heme iron in GD2^{+} xenografts (upper panels) and GD2^{−} xenografts (lower panels) 24h after injection of BNF or anti-GD2-BNF. **D** and **E**. Spectrophotometry of iron content (averages ± SE, n as in legend 6A) in brain (Br), skeletal muscle (Mu), skin (Sk), endocardium (He), kidney (Ki), lung (Lu), liver (Li), spleen (Sp) at background levels and 24h after injection of BNF or anti-GD2-BNF.
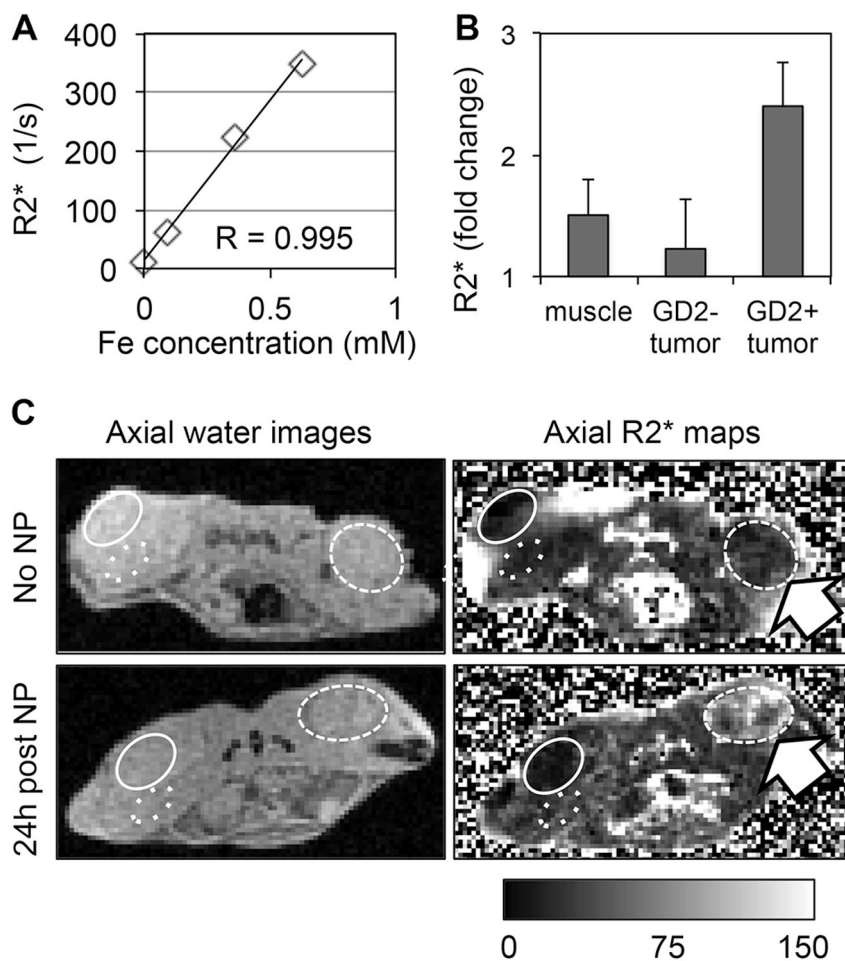
**Figure 7. Iron oxide nanoparticles in GD2 positive xenografts are detectable by magnetic resonance**

**A**. Correlation between MR R2* values iron concentration for BNF nanoparticle phantoms (linear regression, coefficient R=0.995). **B**. R2* fold change in GD2$^+$ tumors, GD2$^-$tumors and muscle in mice 24h after anti-GD2-BNF injection vs. mice with no treatment. Averages ± SD, n=2. **C.** MR images (method parameters B) of a non-injected mouse (upper panels) and a mouse 24h after intravenous anti-GD2-BNF nanoparticle (NP) administration shows elevated R2* for the injected mouse in the GD2$^+$ tumor (arrow). ROI defined on water images (left panels), and corresponding R2* images (right panels) circumscribe GD2$^+$ xenografts (CHLA-20, dashed line) GD2$^-$ xenografts (PC-3, solid line), and control skeletal muscle (dotted). Representative images of 2 experiments with 2 separate anti-GD2-BNF batches.